Efficient hydrogen production from ethanol steam reforming over La-modified ordered mesoporous Ni-based catalysts

Hongyan Ma, Liang Zeng, Hao Tian, Di Li, Xiao Wang, Xinyu Li, Jinlong Gong[*]

Key Laboratory for Green Chemical Technology of Ministry of Education, School of Chemical Engineering and Technology; Collaborative Innovation Center of Chemical Science and Engineering, Tianjin University, Tianjin 300072, China

ABSTRACT

This paper describes the synthesis of a group of meso-xLaNiAl catalysts with ordered mesostructure and La promoters, and their catalytic performance for hydrogen production from ethanol steam reforming. For comparison, the conventional 0LaNiAl catalyst was prepared by impregnation with γ-Al$_2$O$_3$. The characterization results exhibited that meso-xLaNiAl materials possessed excellent textural properties, such as high specific surface areas, large pore volumes and uniform pore sizes. The ordered mesostructure was beneficial to obtain and maintain the 4–6 nm Ni nanoparticles, which were smaller than that of the conventional 0LaNiAl catalyst ($\sim$10 nm). Consequently, meso-xLaNiAl catalysts exhibited superior initial activity with respect to the reference 0LaNiAl catalyst, especially at higher temperatures (873 and 973 K). Particularly, the meso-3LaNiAl catalyst gained the highest amount of easily reduced Ni species and then the highest active surface areas. In addition, the highest initial activity at 873 K is exhibited over meso-3LaNiAl catalyst, which is mainly attributed to the highly dispersed nickel nanoparticles and abundant active surface areas. The meso-3LaNiAl catalyst also exhibited excellent long-term stability. Besides the excellent textural properties, the presence of La-modifiers enhanced the basicity of the catalyst, strengthened the metal-support interaction and cleaned the deposited carbon, resulting in the suppression of carbon deposition and the improvement of stability.

© 2015 Elsevier B.V. All rights reserved.

1. Introduction

Nowadays, the limited reserves and environmental concerns caused by the utilization of the fossil energy resources have spurred extensive attention from the scientific, governmental and industrial communities toward the search for alternative green fuels. Hydrogen is a promising clean energy carrier that can be used directly in an internal combustion engine or a fuel cell for efficient electricity generation [1–3]. In this context, a number of researchers focus on the catalytic hydrogen production via steam reforming of ethanol, which can be economically produced from abundant renewable sources such as sugar cane, corn grains and other starch-rich materials [4–6].

To understand the reaction mechanism of ethanol steam reforming (ESR) and to achieve excellent catalytic performance, various catalytic systems have been extensively investigated [7–11]. For example, Palma et al. [10,11] utilized the CeO$_2$ supported catalysts to study the possible reaction pathways involved

in ESR. Particular attention has been paid to noble metal-based catalysts, such as Pt and Rh, which can effectively break C—C bonds [7,12]. Compared to the high cost of noble metals, the nickel-based catalysts, as the classic catalysts in the methane steam reforming with high activity and relatively low cost, seem to be an excellent alternative. However, there exists severe deactivation due to the thermal sintering and carbon deposition over Ni-based catalysts [13–16]. Therefore, the development of a robust catalyst with excellent catalytic activity, stability, anti-coking and anti-sintering properties is highly desirable.

Previous studies have shown that small Ni particles (<7 nm) were beneficial to the reforming reaction, which could provide more surface active nickel atoms and could effectively inhibit the carbon deposition [17,18]. However, maintaining a high dispersion of metallic particles is a challenging task because Ni particles could agglomerate easily under high temperatures due to their low Tammann temperature (863 K) [19,20]. To achieve small and anti-sintering nickel particles, synthesizing catalyst precursors with well-defined structure, such as hexaaluminates [21], solid solutions [22], perovskites [23], has been considered as a promising strategy. Nevertheless, their structural properties, such as low specific surface areas (<100 m^2/g) and small pore volumes, are limited

* Corresponding author. Fax: +86 22 87401818.
  E-mail address: jlgong@tju.edu.cn (J. Gong).

for hosting sufficient active centers for the reactants. Alternatively, the ordered mesoporous material with large surface areas and well-defined structure, has drawn great attention since the 1990s [24]. Specifically, a series of catalysts with silica-based SBA-15 and MCM-41 as support, have been widely designed owing to the confinement effect of the ordered channels [25,26]. However, due to the weak interaction between nickel and silica support, the Ni particles could move out of the mesoporous to the external surface at high temperatures, resulting in severe sintering [27,28].

Compared to the mesoporous silica materials, the ordered mesoporous alumina has great tendency to form strong interaction with metals and thus has been widely applied in catalysis in recent years [29–31]. Typically, the catalysts with Pt incorporated into the alumina framework via one-pot synthesis exhibited superior activity in CO oxidation to that prepared by the conventional impregnation method [32]. Subramanian et al. [33] demonstrated that $CuFe_2O_4$-mesoporous alumina nanocomposites exhibited stable activity for the water–gas shift reaction. It has also been reported that the Ni–Mg–Al and Ni–Ce–Al catalysts with ordered mesostructure, behaved excellent catalytic activity and stability for reforming reactions [31,34].

Furthermore, basic sites generally facilitate the catalysts to achieve excellent catalytic performance, especially the superior stability. Therefore, alkali metal oxides (such as Na_2O, K_2O), alkaline earth metal oxides (such as MgO, CaO), and some rare earth oxides (such as La_2O_3, Sm_2O_3) are usually selected as basic supports or modifiers [8,35–38]. Compared with other basic metal oxides, La_2O_3 has been widely used as an excellent promoter for various catalysts owing to its specific properties [1,23,39–41]. Besides neutralizing the acid sites, the addition of La-promoters typically has the following effects: (i) stabilization of the textural and structural properties of alumina support [42]; (ii) enhancement of the catalytic performance with small metal particles and sufficient active areas [43–45] and (iii) suppression of carbon deposition with improved stability [1,41].

On the basis of the above analysis, it is of interest to investigate the effect of combining ordered mesostructure and La-modification on the catalytic performance of Ni based ESR catalysts. In this work, a group of meso-xLaNiAl catalysts with ordered mesostructure were originally designed and synthesized. Various techniques including X-ray powder diffraction (XRD), N_2 adsorption–desorption, transmission electron microscopy (TEM), H_2 temperature-programmed reduction (TPR), CO_2 temperature programmed desorption (CO_2-TPD), thermogravimetric (TG) analysis and temperature-programmed oxidation (TPO) were carried out to characterize the catalysts. To highlight the superiority of the ordered mesostructure, their catalytic behaviors were compared with the conventional mesoporous Ni/γ-Al_2O_3 catalysts. Moreover, the influence of La-modification on the catalytic performance of the meso-xLaNiAl catalysts is discussed.

2. Experimental

2.1. Preparation of catalysts

Ordered mesoporous meso-NiAl materials were synthesized via a one-pot evaporation induced self-assembly (EISA) method [46–48]. The amount of Ni was fixed to 7 wt% for meso-NiAl materials investigated in this study. The meso-xLaNiAl catalysts were prepared by impregnating La(NO$_3$)$_3$·6H$_2$O on as-prepared meso-NiAl materials, and the lanthanum oxide loadings were 0 wt%, 1.5 wt%, 3 wt%, 6 wt%, and 12 wt%, respectively, (denoted as x = 0, 1.5, 3, 6, 12) [49,50]. In a typical synthetic procedure, approximately 1.0 g of (EO)$_{20}$(PO)$_{70}$(EO)$_{20}$ triblock copolymer and an expected stoichiometric amount of Ni(NO$_3$)$_2$·6H$_2$O were dissolved in 10.0 mL

of anhydrous ethanol with vigorous stirring for at least 5 h for dissolution. A certain amount of aluminum isopropoxide was dissolved in 1.6 mL of 67–70 wt% nitric acid and 7.0 mL of anhydrous ethanol at room temperature. Once dissolved, the two solutions were combined and 3.0 mL of anhydrous ethanol was employed to thoroughly transfer the aluminum isopropoxide solution. The combined solution was continuously stirred for another 8 h. The mixture was placed in the oven at 333 K for solvent evaporation for 48 h. Calcination was carried out by slowly increasing the temperature from room temperature to 973 K with a ramping rate of 1 K/min and keeping the temperature for 5 h in an air flow. The obtained material was labeled as meso-NiAl. The as-prepared meso-NiAl was incipient wetness impregnated with a certain amount of La(NO$_3$)$_3$·6H$_2$O. The resultant catalyst precursors were dried at room temperature for 24 h, and calcined at 973 K for 2 h. The final materials were labeled as meso-xLaNiAl.

For comparison, a conventional 7 wt% Ni/γ-Al_2O_3 was also prepared via incipient wetness impregnation. The commercial γ-Al_2O_3 power was impregnated with Ni(NO$_3$)$_2$·6H$_2$O aqueous solution, followed by drying at room temperature for 24 h and calcinating at 823 K for 5 h.

2.2. Characterization

XRD patterns were performed with a Rigaku D/MAX-2500 diffractometer employing the graphite filtered Cu Kα radiation ($\lambda = 1.54056$ Å), over a 2θ range of 0.6–5.0° (low angel range) and 10–80° (wide angle range).

The nitrogen adsorption and desorption isotherms were obtained with Micromeritics TriStar 3000 at 77 K. Prior to the tests, all the materials were degassed at 573 K for 3 h. The specific surface areas were obtained from the isotherms using the BET method. The average pore diameters and pore volume were calculated by the BJH method from the desorption branches of the isotherms. Pore size distributions were calculated using the adsorption regimes of the isotherms.

Morphologies of catalysts were characterized using a JEM-2100F transmission electron microscope under a working voltage of 200 kV, which was equipped with a liquid nitrogen cooled energy-dispersive X-ray spectroscopy (EDS) detector for elemental analysis. The powder were first dispersed in ethanol by ultra-sonication and then supported on a copper grid-supported transparent carbon foil.

TPR measurement was performed on a Micromeritics Autochem II 2920 instrument. In a typical experiment, the sample (100 mg) was first pretreated at 673 K for 1 h in flowing Ar (30 mL/min) to remove moisture and impurities. After cooling to 323 K, a 10 mol% H_2–Ar (30 mL/min) gas mixture was introduced. The catalyst was heated to 1223 K at a rate of 10 K/min and the TCD signal was recorded continuously.

H_2 pulse chemisorption was also performed over Micromeritics Autochem II 2920 instrument to measure the active nickel surface areas. The samples were reduced at 973 K for 1 h under 10% H_2/Ar flow (30 mL/min) and then were cooled down to 323 K. The chemisorption was carried out by pulsing of a mixture of 10% H_2/Ar (30 mL/min). The nickel surface areas was calculated from the volume of H_2 adsorbed assuming the stoichiometric ratio $H_{adsorbed}$/$Ni_{surface} = 1$ and that a density of active sites on the surface of 1.54×10^{19} atoms/m^2 [51].

CO_2-TPD analyses were also evaluated on the same apparatus as described for TPR. The sample (100 mg) was pretreated at 473 K for 0.5 h in an Ar stream (50 mL/min) and then cooled down to 333 K. A stream of pure CO_2 (50 mL/min) gas was introduced. The sample was purged with a He stream at 393 K until the baseline of CO_2 in the mass spectrum reached steady state. Finally, the CO_2-TPD

was carried out with a ramping rate of 10 K/min from 393 K to the needed temperature under a He stream (30 mL/min).

TG was carried out to study the properties of carbon deposition over spent catalysts using a thermal gravimetric analysis system (STA449F3, NETZSCH Corp.). The sample was heated in a flow of air (50 mL/min) with a heating rate of 10 K/min up to a final temperature of 1073 K.

TPO profiles of the spent catalysts were obtained from the same apparatus as described for TPR. Typically, the samples were pretreated at 473 K for 0.5 h under an Ar stream and then cooled down to 393 K. Finally, the TPO was performed with a ramping rate of 10 K/min from 393 K to the needed temperature under a 10 mol% O_2–He stream (50 mL/min) and the MS signal was recorded continuously.

2.3. Catalytic test in ESR

The catalytic activity tests were performed under atmospheric pressure in a fixed-bed tubular quartz reactor ($\Phi 8 \times 30$ mm). Typically, 50 mg catalyst was diluted with 1 mL quartz particles. Prior to each reaction, the catalyst was reduced in situ in a mixed flow of H_2 (10 mL/min) and N_2 (90 mL/min) at 973 K for 1 h to obtain sufficient Ni metal. Before introducing the feed gas, the catalyst bed was purged with N_2 for half an hour to remove the absorbed hydrogen. The bed was turned to the designed temperature, the liquid solution with water/ethanol molar ratio of 8 was fed into a vaporizer (423 K) by a HPLC pump (P230, Elite, China). An inert N_2 flow was also introduced into the vaporizer to help carrying the feed vapor into the reactor and to dilute the feed gas. Partial pressure of ethanol was maintained constantly at 4% for all the experiments. The product gas was analyzed on-line by a GC (Agilent 7890A) equipped with two detectors, namely FID and TCD. Also, the GC was equipped with a Porapack-Q column for analyzing possible organic species (e.g., methane, ethylene, acetaldehyde, ethanol, and acetone) and a TDX-01 column to analyze the incondensable gas like H_2, CO_2, CH_4, CO. For the initial activity test, the reaction temperature decreased from 973 K to 673 K in 100 K increments to minimize the influence of the carbon deposition and the results were obtained in steady-state condition. Furthermore, the stability test was carried out at 873 K.

Ethanol conversion and selectivity of different products were calculated as follows [52,53]:

$$X_{EtOH}(\%) = \frac{F_{EtOH, in} - F_{EtOH, out}}{F_{EtOH, in}} \times 100 \quad (1)$$

$$S_{H_2}(\%) = \frac{1}{6} \times \frac{moles(H_2)produced}{moles(EtOH)feed \times X_{EtOH}} \times 100$$

$$or \ S_{H_2}(\%) = \frac{1}{6} \times \frac{F_{H_2, produced}}{F_{EtOH, in} \times X_{EtOH}} \times 100 \quad (2)$$

$$S_j(\%) = \frac{(\%j) \times i}{\sum ((\%j) \times i)} \times 100 \quad (3)$$

where F represents the molar flow rate of EtOH or H_2, and j represents the carbon containing species in the products, including CH_4, CO, CO_2, C_2H_4, C_2H_6, CH_3CHO, and CH_3COCH_3. In addition, i is the number of carbon atoms in the carbon containing species.

3. Results and discussion

3.1. Characterization of calcined catalysts

Low-angle XRD patterns of calcined samples are shown in Fig. 1(a). All meso-xLaNiAl samples demonstrate diffraction peaks around $2\theta = 0.7$–$0.9°$ and weak diffraction peaks at approximately

1.4°, which could be indexed as the reflection of (1 0 0) and (1 1 0) planes in the $p6mm$ 2D hexagonal ordered structure, respectively [47]. In addition, the position of (1 0 0) diffraction peaks of meso-xLaNiAl ($x \neq 0$) changes slightly compared with meso-0LaNiAl. Those observations confirm that the ordered mesoporous Ni–Al materials were successfully synthesized and the ordered mesostructure was preserved during the impregnation process despite the introduction of lanthanum species. In contrast, 0LaNiAl sample shows no diffraction peak at low angles, suggesting no ordered mesoporous structure exists in the conventional catalyst.

Fig. 1(b) presents the wide-angle XRD (WXRD) patterns of several selected catalysts. The patterns for all the shown meso-xLaNiAl samples exhibit mainly two wide diffraction peaks, which are corresponding to amorphous Al_2O_3 [29]. No peaks associated with nickel species are found, indicating the high dispersion of Ni species inside the framework of the materials due to the advantages of the one-pot method [54]. Moreover, no La_2O_3 characteristic peaks are observed for meso-xLaNiAl catalysts, indicating lanthanum species are either amorphous or well dispersed. The observation is consistent with the result that lanthanum ions formed an atomic layer on alumina for loadings up to 8.5 μmol La/m^2 alumina support [55]. For 0LaNiAl, the pattern is different from the ordered mesoporous samples, exhibiting the intense peaks of γ-Al_2O_3 at 46.8° and 66.7° (JCPDS Card No. 10-0425) and the apparent diffraction peak at 43.2° associated with the NiO nanoparticles (JCPDS Card No. 47-1049). However, it is difficult to judge the presence of the $NiAl_2O_4$ phase because its characteristic peaks at 37.1° and 65.5° are similar with these of γ-Al_2O_3 and NiO. In a word, these results indicate apparent NiO particles formed on γ-Al_2O_3 with poor dispersion for 0LaNiAl catalyst.

Nitrogen physisorption isotherms of as-synthesized materials are displayed in Fig. 2. For all meso-xLaNiAl materials, the isotherms reveal IV type isotherms with H1-type hysteresis loops, which indicate the presence of the uniform "cylindrically shaped" channels [56]. All the capillary condensation steps of the hysteresis loops are steep, suggesting the excellent uniform mesopores among the framework. In comparison, 0LaNiAl sample exhibits IV H2 typed hysteresis loops, which is the typical feature of mesopores with "ink bottle" shapes.

In addition, the pore size distributions of meso-xLaNiAl samples in Fig. 2(b) are all narrow and the main peaks are located in the range of 9–12 nm, indicating the presence of the large percentage of the mesopores, along with little amount of micro and macropores. Moreover, the maximum value of pore diameters increases with the increased lanthanum content and meso-12LaNiAl sample possesses the largest value around 11.2 nm. On the contrary, the pore size distribution for 0LaNiAl is extremely wide.

The textural properties of samples are summarized in Table 1. All the samples possess relatively high specific surface area up to 280 m^2/g and large pore volume up to 0.63 cm^3/g. Furthermore, for meso-xLaNiAl materials, the specific surface area and pore volume slightly decrease with the increasing of lanthanum content, while the average pore diameter becomes larger with the La-modification. The results suggest that, surface and structure rearrangement occurred due to the incorporation of La, which will be further discussed with TPR. The conventional 0LaNiAl sample has smaller surface area and pore volume than meso-xLaNiAl samples. Overall, the ordered mesoporous materials have uniform mesopores, high specific surface areas and large pore volumes, which promise their potential applications as catalysts.

TEM images of representative catalysts are shown in Fig. 3. For 0LaNiAl material, some small nanoparticles are apparently located on the γ-Al_2O_3 surface, which correspond to NiO particles. In the case of meso-xNiLaAl catalysts, the cylindrical channels along the (1 1 0) and (0 0 1) directions are distinctly observed further confirming the presence of the typical ordered mesostructure. The results
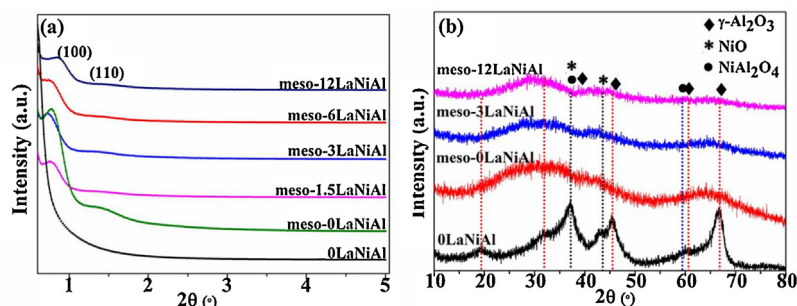
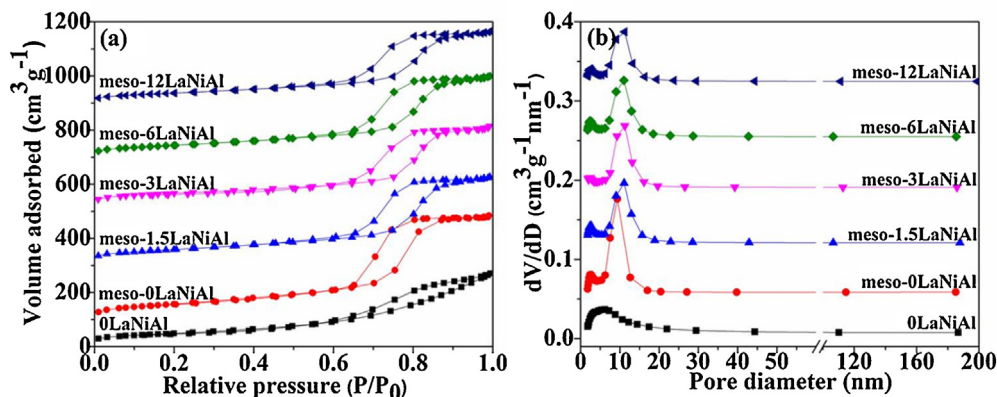**Fig. 1.** Low-angle (a) and wide-angle (b) XRD patterns for calcined samples.

Fig. 2. Nitrogen adsorption–desorption isotherms (a) and pore size distributions (b) of various samples.

Table 1
Textural properties of the catalysts.

Sample	Specific surface areas (m²/g)	Pore volume (cm³/g)	Average pore diameter (nm)	Isotherm type	Nickel crystalline size (nm)[a]	Active nickel surface areas (m²/g_Ni)[b]
0LaNiAl	175	0.42	8.9	IV H2	9.6/10.7	5.3
Meso-0LaNiAl	280	0.63	8.8	IV H1	5.0/5.4	9.5
Meso-1.5LaNiAl	209	0.52	9.4	IV H1	5.4	11.1
Meso-3LaNiAl	202	0.48	9.5	IV H1	4.4/4.6	16.9
Meso-6LaNiAl	195	0.48	9.5	IV H1	4.7	13.9
Meso-12LaNiAl	167	0.43	9.8	IV H1	4.6	9.9

[a] Derived from diffraction line in XRD corresponding to the Ni (1 1 1) plane at 44.5° for the reduced/spent catalysts.
[b] Determined by H_2 pulse chemisorption.

are in good agreement with the intense XRD peaks at low angles and the H1-type hysteresis loops in nitrogen adsorption–desorption isotherms. In addition, the observations indicate that the ordered mesostructure reveals excellent thermal stability, which though suffered from the impregnation of lanthanum oxide and the subsequent calcination (973 K for 2 h). Moreover, all meso-xLaNiAl samples show no apparent nanoparticles in the TEM images, demonstrating the nickel oxide and lanthanum oxide are highly dispersed throughout the whole structure.

TPR profiles of the as-prepared catalysts are shown in Fig. 4 and quantification of TPR data are summarized in Table 2. As it is observed in Fig. 4, only one pronounced reduction peak in the range of 673–1173 K is displayed over 0LaNiAl catalyst, which derived from the reduction of nickel species with different degrees of interaction with the alumina support [45]. After deconvolution, three reduction peaks are shown: (i) the reduction at 851 K is related to the reduction of nickel species with weak interaction with support [57]; (ii) non-stoichiometric amorphous nickel aluminates are attributed to the reduction temperature at 935 K [58]; (iii) the nickel species that strongly interacted with the support, like a diluted $NiAl_2O_4$ phase, could be reduced at 1024 K [1,59]. Almost similar profile is obtained over meso-0LaNiAl catalyst and the Ni atoms embedded in alumina skeleton primarily contributed to the reduction peak [60,61]. Differently, "free" or dissociated NiO, which was not bound with the support [59,61,62], is presented over La-containing catalysts. The incorporation of La also increases the proportion of NiO (peak at 828–889 K) with weak metal-support interaction, and decrease the proportion of nickel species in Ni–Al skeleton (peak at 961–998 K). The highest amount of these nickel species (~37.7%) that were not or weakly interacted with the support were obtained over the meso-3LaNiAl sample. Additionally, over meso-xLaNiAl ($x \neq 0$) catalysts, the reduction temperatures of the nickel species that embedded in Ni–Al skeleton and that strongly interacted with alumina support migrate to higher temperatures than meso-0LaNiAl, indicating the strengthened metal-support interaction.

Reported by Serrano-Lotina et al. [63], the TPR results of hydrotalcite-like compounds presented that, the increase of Mg/Al molar ratio shifted the first peak toward lower temperature and the second peak toward higher temperature owning to a
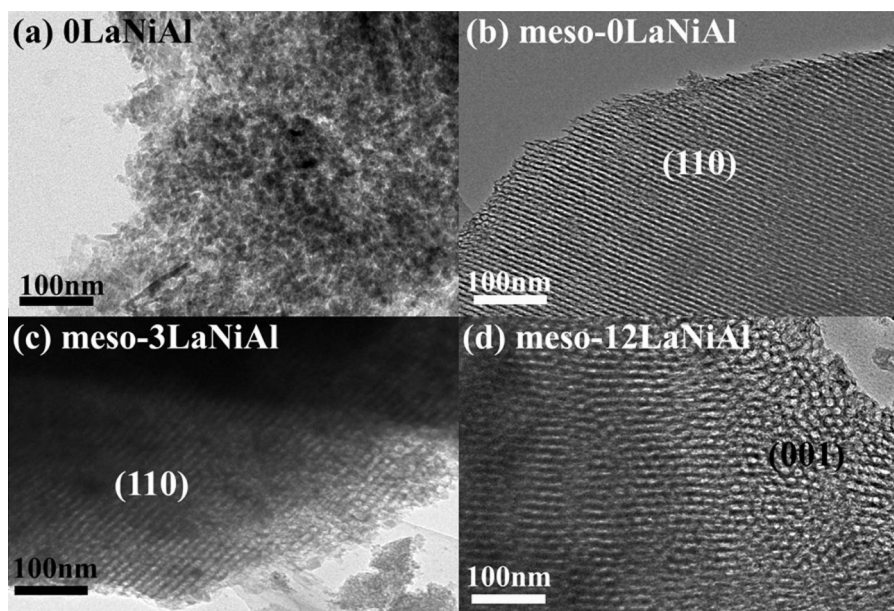
Fig. 3. TEM images of calcined samples.

Table 2
Quantitative TPR data of calcined catalysts.

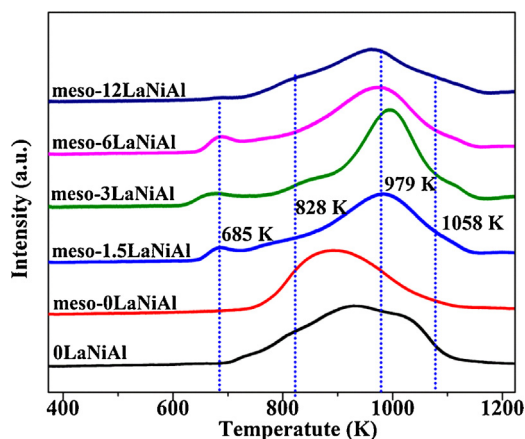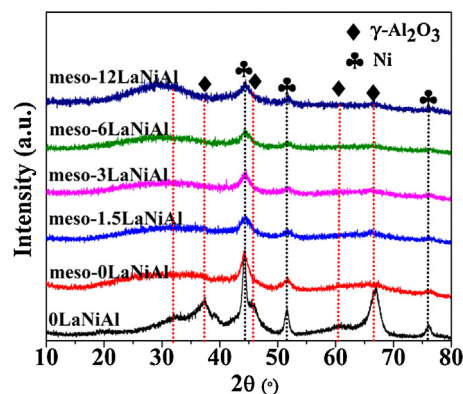| Sample	"free" NiO	NiO–Al	Surface NiAl$_2$O$_4$[a]/Ni-Al skeleton[b]	NiAl$_2$O$_4$
0LaNiAl	–	851 K, 39%	935 K, 30%	1024 K, 31%
Meso-0LaNiAl	–	850 K, 9.5%	908 K, 84%	1036 K, 6.4%
Meso-1.5LaNiAl	685 K, 3.0%	828 K, 25%	979 K, 65%	1058 K, 6.0%
Meso-3LaNiAl	682 K, 5.7%	889 K, 32%	998 K, 57%	1100 K, 4.9%
Meso-6LaNiAl	690 K, 3.9%	846 K, 30%	974 K, 61%	1058 K, 4.8%
Meso-12LaNiAl	697 K, 0.5%	836 K, 24%	961 K, 63%	1080 K, 12%

[a] Surface NiAl$_2$O$_4$ is for 0LaNiAl catalyst.
[b] Ni–Al skeleton is for meso-xLaNiAl catalysts.

Fig. 4. H$_2$-TPR profiles of various samples.

Fig. 5. Wide-angle XRD patterns of various reduced samples.

strengthened interaction on the Mg–Ni–Al surface. Additionally, according to [1,64], the lanthanum element could incorporate into the alumina framework. In our case, it is reasonable to speculate that La could serve as a similar role as Mg in strongly interacting with the alumina framework, and concurrently destroy the metastable state of Ni–Al mixed oxide. Therefore, nickel species that could be easily reduced and that could strongly interact with support, were obtained simultaneously during the La incorporation.

3.2. Characterization of reduced catalysts

Crystalline phases of catalysts reduced at 973 K were examined by WXRD and the results are displayed in Fig. 5. The meso-xLaNiAl catalysts show two weak board diffractions peaks (at 21.3–36.3° and 62.3–66.7°) corresponding to amorphous alumina phase, similar with the patterns of the as-synthesized samples. No intense diffraction peaks corresponding to any lanthanum species are found in all the La-containing catalysts, suggesting no apparent lanthanum oxide nanoparticles formed after vigorous reduction. Furthermore, for 0LaNiAl catalyst, the diffraction peaks (at 31.8°, 37.5°, 45.7°, 66.7°) attributed to γ-Al$_2$O$_3$ are displayed apparently.
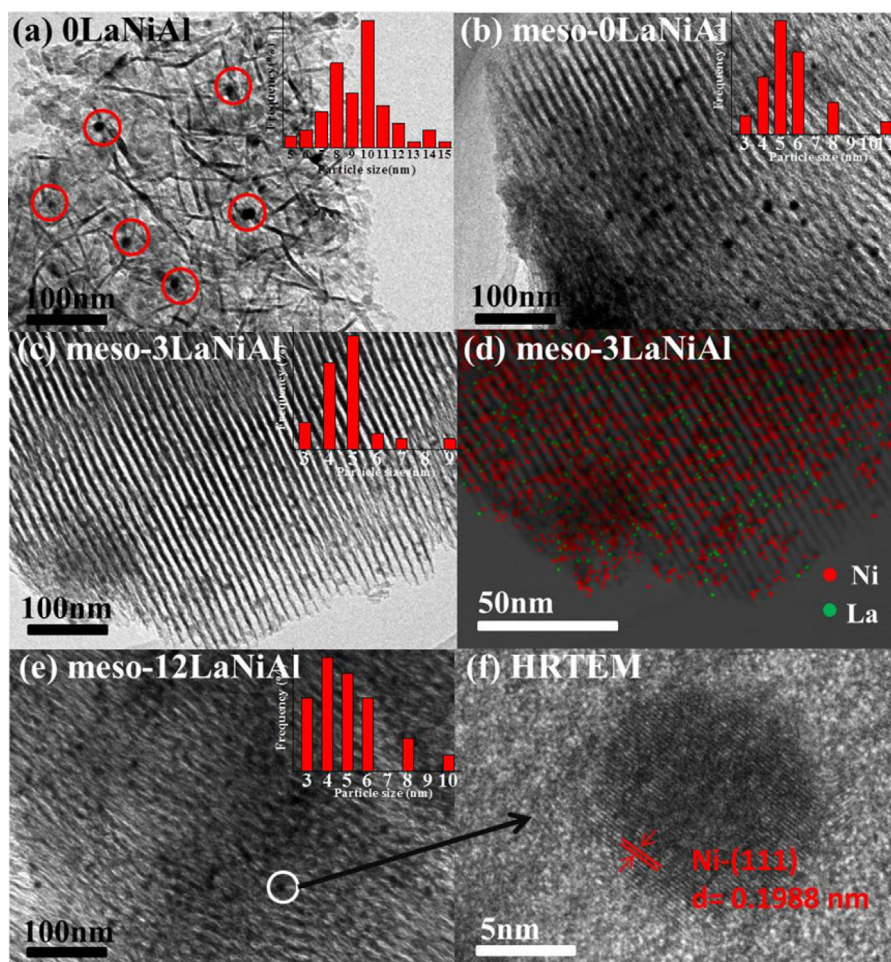
Fig. 6. TEM images of reduced samples and EDS elemental maps of meso-3LaNiAl sample.

Moreover, all the patterns of the reduced catalysts demonstrate obvious diffraction peaks at 44.3°, 51.7° and 76.3° assigned to metallic Ni phases (JCPDS Card No. 87-0712) indicating some nickel particles have been reduced from the Ni–Al framework. The average crystalline sizes of Ni nanoparticles were calculated using the Scherrer equation based on diffraction peaks of nickel with (1 1 1) plane (Table 1). The crystal size for meso-xLaNiAl is quite small (about 4–6 nm) suggesting the high dispersion of nickel particles. In comparison, over 0LaNiAl samples without ordered structures, the average crystal size of Ni particles is about 9.6 nm. Therefore, we could conclude that small Ni particles could be obtained due to the confinement effect of the ordered mesostructured over reduced meso-xLaNiAl catalysts.

TEM images of reduced catalysts and corresponding EDS elemental maps are displayed in Fig. 6. For the conventional 0LaNiAl catalyst, obvious nanoparticles around 10.0 nm are clearly presented upon reduction, attributed to Ni particles based on WXRD results. In addition, in the case of meso-xLaNiAl catalysts, small nanoparticles are uniformly dispersed among the catalysts. The nanoparticles are Ni particles according to the HRTEM image of representative particle with a d -spacing of 0.1988 nm. This finding suggests that the Ni species were reduced from the framework and embedded in the wall of pores simultaneously. The phenomenon is consistent with the observation that no nanoparticles are shown in TEM images before reduction. The average Ni particle size of randomly picked for x = 0, 3, 12 over the meso-xLaNiAl samples is 5.7 nm, 5.2 nm and 5.4 nm, respectively. All of them varied in a much narrow range, suggesting that the nickel particle sizes of the

meso-xLaNiAl catalysts are almost similar, and they are all smaller than that of 0LaNiAl catalyst. For meso-3LaNiAl as representative, the EDS image (Fig. 6(d)) shows that the lanthanum species and nickel species are presented homogeneously in the sample and the homogenous element distribution would enlarge the interfacial perimeter, enhancing the metal-support interaction [65].

In addition, H_2 pulse chemisorption was carried out to evaluate the amount of active nickel surface areas and the results are listed in Table 1. It can be observed that meso-0LaNiAl catalyst with ordered mesostructure presents larger active surface areas than 0LaNiAl catalyst, which is consistent with its smaller nickel particle size. For meso-xLaNiAl catalysts, the La-modification significantly affects the active nickel surface areas with negligible changes of nickel particle size. It presents an upward trend with the increase of x to 3 and then decrease with x increasing from 3 to 12. Such trend is consistent with that of the amount of the nickel species with weak interaction with the support. The reason may be that the nickel particles obtained from the reduction of these easily reduced nickel species could be less embedded in the framework and thus expose more active surface atoms. Similar results have been obtained and analyzed by Wang et al. [66].

3.3. Catalytic activity in ESR

The initial catalytic activity tests of all catalysts in the ESR were performed from 673 K to 973 K, aiming to examine the parameters that affect the catalytic performance. Since the ethanol conversion and hydrogen selectivity are the main parameters to be taken into

account for practical use of ESR catalysts, here both of them are selected for comparison and shown in Fig. 7(a) and (b). The corresponding thermodynamic equilibrium was evaluated using the HSC software and also shown in the same figure.

It can be clearly seen that the catalytic performance over various catalysts is complicated at different reaction temperature which also reported in previous literatures [67–69], and that could be attributed to both the effect of metal and support [9,41,70]. At 673 and 773 K, all catalysts exhibit low ethanol conversion and H_2 selectivity as well as the presence of C_2 products (C_2H_4 and CH_3CHO, not shown) which indicated Ni metal had weaker capability of breaking the C—C bond at low temperatures. Additionally, H_2 selectivity of the meso-xLaNiAl catalysts ($x \neq 0$) is higher than that of 0LaNiAl and meso-0LaNiAl catalysts, associated with less C_2 products. Sanchez Sanchez et al. [1,41] and Fatsikostas et al. [9] demonstrated that, lanthana could promote ethanol dehydrogenation reaction and hinder dehydration of ethanol and thus produce quantities of hydrogen produced from decomposition of CH_3CHO on Ni. Therefore, the catalytic activity at low temperatures resulted from the integrated effect of metal and support. At 873 K and 973 K,

almost complete ethanol conversion and high H_2 selectivity are achieved over all catalysts, and some CH_3CHO were detected for 0LaNiAl while little for meso-xLaNiAl catalysts. At higher temperatures, the nickel metal obtained enhanced capability for C–C cleavage [71] which thus facilitated converting the intermediates (e.g., C_2H_4 and CH_3CHO) to H_2 through reforming reaction pathways [72,73], and consequently primarily accountant for the higher activity. Additionally, meso-xLaNiAl catalysts exhibit significantly enhanced catalytic performance than 0LaNiAl catalyst at higher temperatures, primarily due to the excellent catalytic capacity of nickel metal.

Particularly, the effect of ordered mesostructure and La-modification is much more obvious at high temperatures. As the catalytic performance at 973 K is limited by thermodynamics, product distribution at 873 K is shown in Fig. 7(c). With the presence of ordered mesostructure, meso-xLaNiAl catalysts exhibit higher H_2 selectivity than 0LaNiAl catalyst. For meso-xLaNiAL catalysts, the H_2 selectivity follows a volcano trend with increasing La content and the highest selectivity is obtained over meso-3LaNiAl catalyst. It can also be found that with the higher H_2 selectivity, higher CO_2 selectivity and lower CO selectivity are also exhibited. Since the CO_2/CO ratio has been considered as an indicator for water gas
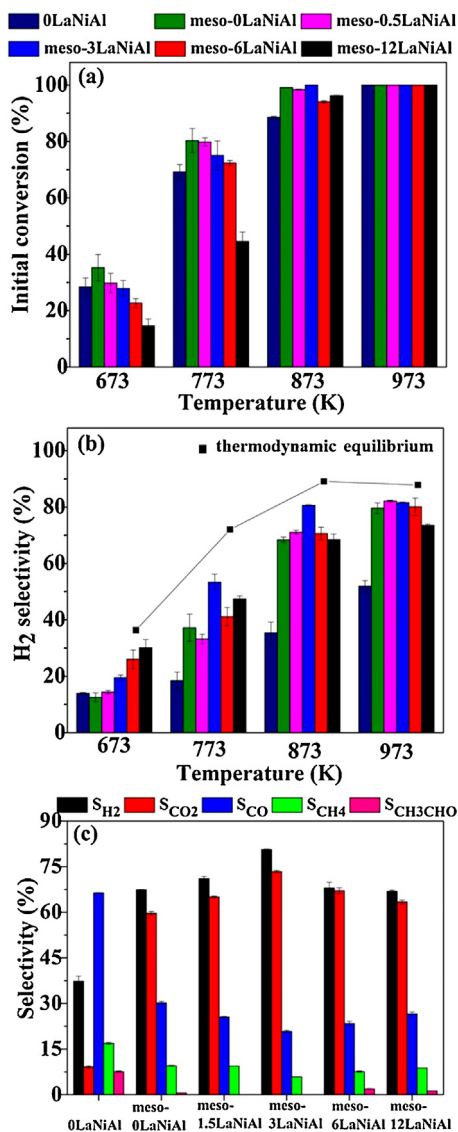

Fig. 7. Initial catalytic activity of various catalysts in ESR: ethanol conversion (a), hydrogen selectivity (b) at different temperatures, and product distribution at 873 K (c). Reaction conditions: ethanol feed velocity, 3.7 g_{cat} h/mol for 673, 773 K, 1.9 g_{cat} h/mol for 873, 973 K; 4 vol% of ethanol in gas; S/C = 4, 1 atm.
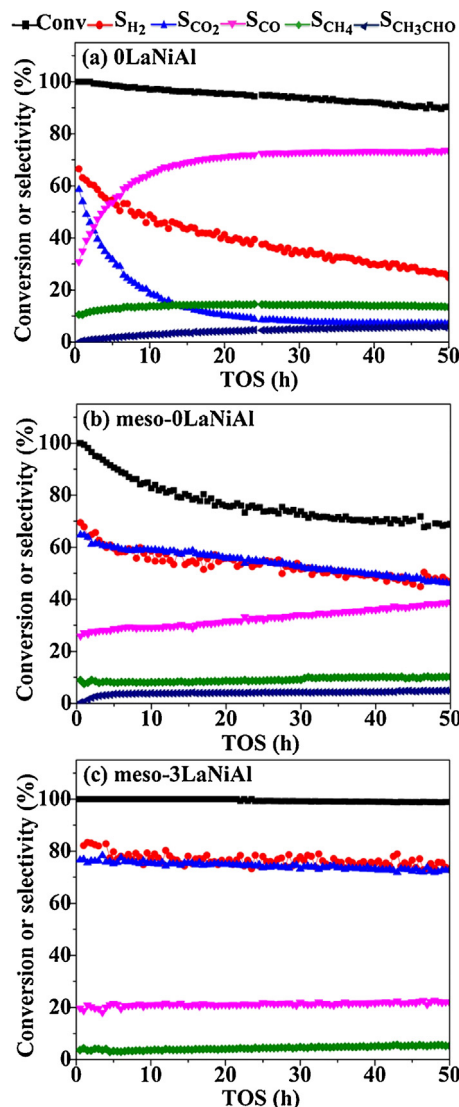

Fig. 8. Stability performance over three catalysts. Reaction conditions: ethanol feed velocity, 2.5 g_{cat} h/mol, 873 K, 4 vol% of ethanol in gas; S/C = 4, 1 atm.

shift reaction (WGSR, $CO + H_2O \rightarrow CO_2 + H_2$) activity, the enhanced H_2 selectivity is probably related to the catalysts' capability to facilitate WGSR reaction [72,74]. Combined with the characterization results, it can be clearly observed that the trend of the catalytic performance matches well with that of the active nickel surface areas and nickel metal dispersion. Indeed, the catalytic activity of ESR is highly affected by the amount of Ni sites [75–77]. The meso-3LaNiAl catalyst exhibits the highest active surface area as shown in Table 1 and hence delivers the highest initial activity. Yet, not enough Ni sites could be provided by 0LaNiAl catalyst to cleave all the C—C bonds, and hence relatively high selectivity of CH_3CHO is detected.

3.4. Stability test in ESR

To better understand the effect of the ordered mesostructure and La-modification in ESR, 0LaNiAl and meso-0LaNiAl as well as meso-3LaNiAl catalysts were screened out with a 50 h stability test at 873 K, and the results are displayed in Fig. 8. For 0LaNiAl catalyst, the ethanol conversion decreases slightly together with increasing selectivity of aldehyde, indicating a loss of the catalyst's capability to facilitate C—C bond cleavage. In addition, the H_2 selectivity suffers significant deactivation, accompanied by the decrease of CO_2 selectivity and the rise of the CO selectivity. The observation suggests that the activity for WGSR was severely weakened upon reaction. Deactivation also happens for meso-0LaNiAl catalyst. The conversion of ethanol decreases gradually from 100% to 68% and the H_2 selectivity reduces to 48% eventually. Obviously, the changes of the selectivity toward H_2 and other C-containing products over meso-0LaNiAl catalyst are moderate than that of 0LaNiAl, which might be owing to their ordered structural properties for maintaining smaller nickel particles and achieving more "accessible" Ni active sites. With La-addition, the catalyst shows enhancement in the catalytic performance and long-term stability. Notably, the activity and selectivity towards different products remain almost constant throughout the 50 h reaction, such as 100% ethanol conversion and 79% hydrogen selectivity. It is the incorporation of lanthanum that contributed to this result compared to meso-0LaNiAl catalyst. Sanchez Sanchez et al. [1] reported superior catalytic performance on $Ni/La-Al_2O_3$ to that on Ni/Al_2O_3 in ESR and it has been widely reported that the La-promoter could improve the catalytic stability in various reforming reactions [78–80]. Notably, for all the catalysts, no ethylene was detected, which might be converted through polymerization and/or reforming pathway. Active metal sintering and carbon deposition are the primary reasons for catalyst deactivation in ESR, both of which will be investigated and compared among the three spent catalysts.
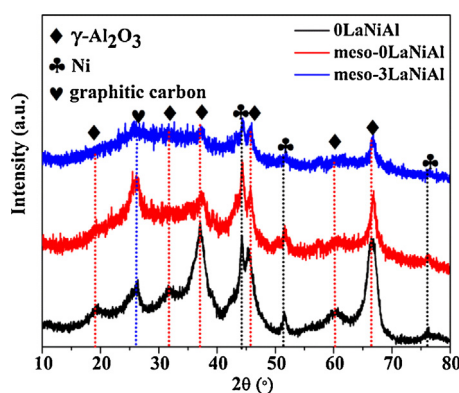
3.5. Deactivation analysis

The spent catalysts after 50 h of stability test were characterized by various techniques to investigate the factors resulting in different stability performance.

WXRD patterns of spent catalysts upon the stability test are presented in Fig. 9. Diffraction peaks assigned to $\gamma-Al_2O_3$ phase are shown in all the samples, indicating the presence of phase transition from amorphous to $\gamma-Al_2O_3$ for the alumina framework over the meso-xLaNiAl catalysts. The intensities of those $\gamma-Al_2O_3$ peaks for $x = 3$ are slightly weaker than the peaks for $x = 0$, suggesting the La-promoter enhanced the thermal stability of alumina skeleton. In addition, all the catalysts present characteristic diffraction peaks corresponding to nickel metal and the average Ni crystallite sizes decrease in the following sequence: 0LaNiAl (10.7 nm) > meso-0LaNiAl (5.4 nm) > meso-3LaNiAl (4.6 nm). As shown in Table 1, the particle sizes show negligible changes after the stability tests, indicating excellent anti-sintering performance due to the strong metal-support interaction and the confinement effect of the mesostructure. Moreover, the strong diffraction peaks around 26.5° are attributed to the graphitic carbon (JCPDS Card No.41-1487), indicating a considerable amount of graphitic carbon was deposited on 0LaNiAl catalyst and meso-0LaNiAl catalyst. In comparison, meso-3LaNiAl catalyst shows weaker diffraction peak about graphitic carbon, suggesting less graphitic carbon accumulated on the surface of the La-modified catalyst.

The properties of the deposited carbon over spent catalysts were characterized by TG as depicted in Fig. 10. The TG curves of samples exhibit a slight rise in the region of 573 K to 723 K, which might result from the oxidation of the metallic Ni [61]. Furthermore, the mass loss percentage of catalysts decreases in the following sequence: 0LaNiAl (17.0%) > meso-0LaNiAl (14.3%) > meso-3LaNiAl (11.4%). TPO was also carried out to confirm the order as shown in Fig. 11. By quantifying the peak areas after normalized, the area ratio of 0LaNiAl, meso-0LaNiAl and meso-3LaNiAl is 1:0.86:0.72. The trend is in accordance with that of the TG result.

Additionally, as shown in DTG (Fig. 10 inset) and TPO profiles, the peaks from 472 K to 573 K might be derived from the combustion of amorphous carbon species [61] and the other peaks at higher temperatures could be attributed to the oxidation of graphitic carbon [41,81]. Furthermore, the high temperature peaks at 795–804 K and 870–885 K are further ascribed to the oxidation of carbon near and far from the nickel particles, respectively [82–84]. The high temperature peak around 800 K over the spent 0LaNiAl catalyst, has stronger intensity and larger peak area compared to those of meso-0LaNiAl and meso-3LaNiAl catalysts, indicating more coke was deposited close to the Ni particles and then caused severe deactivation.
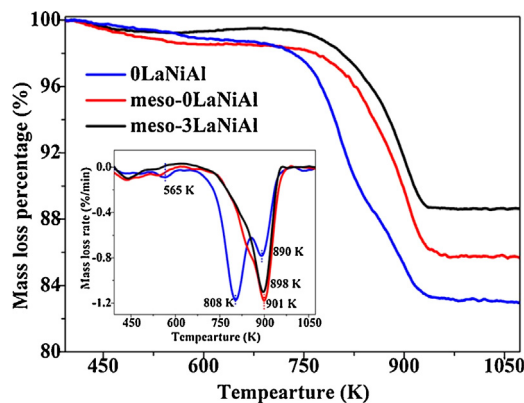

Fig. 9. WXRD patterns of spent catalysts.

Fig. 10. TG and DTG (inset) profiles for various spent catalysts.

Fig. 11. TPO profiles for various spent catalysts.

To further investigate the structure and morphology of used catalysts, TEM micrographs were carried out as shown in Fig. 12. 0LaNiAl catalyst presents large amount of carbon nanotubes, which could widely cover the Ni particles and consequently lead to fast deactivation. Over meso-0LaNiAl and meso-3LaNiAl catalysts, some carbon nanotubes are also formed and mainly distribute outside of the mesopores. Although meso-3LaNiAl catalyst presents carbon nanotubes, it can still provide abundant active sites due to the less amount of carbon and its inherent large amount of active sites, and therefore achieved excellent stability. Additionally, large part of Ni nanoparticles appear to be embedded in the cylindrical channels over meso-0LaNiAl and meso-3LaNiAl catalysts with the average particle size of 5.4 and 4.9 nm, respectively. These observations proof that the confinement effect of the ordered mesostructure could effectively suppress the sintering of Ni particles, thus resulting in the enhanced coking resistance [34]. We can also find that over the meso-0LaNiAl catalyst, larger Ni particle (∼25 nm) embedded on the top of the carbon nanotube. The large Ni particles might be derived from: (i) the aggregation of some Ni–Al nanoparticles from the destroyed framework shown in Fig. 12(c); (ii) the sintering of the small Ni nanoparticles which migrated out of the internal channels due to the relative weak metal-support interaction [31]. The movement and sintering of Ni particles over meso-3LaNiAl were effectively suppressed as shown in Fig. 12(e), owing to the anchoring effect of the species strongly interacted with the support
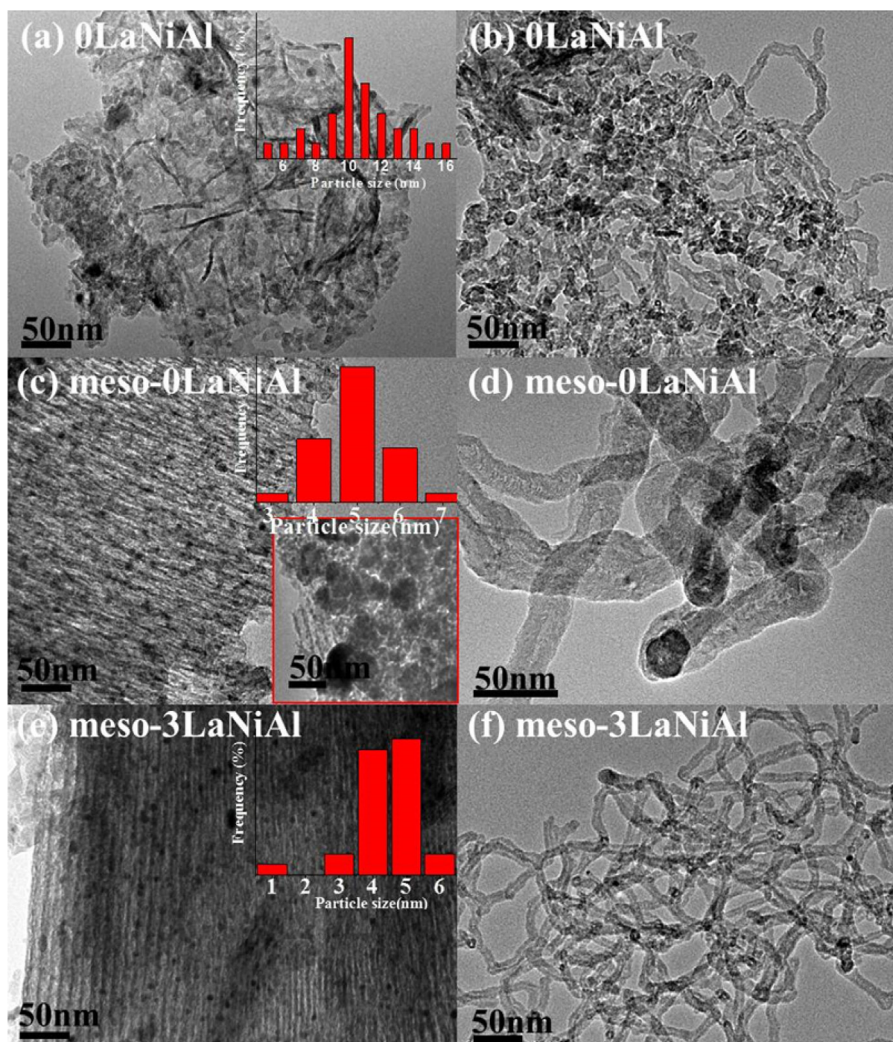
Combining the results from TG, DTG and TPO, we can conclude that meso-0LaNiAl exhibits lower amount of carbon deposition than 0LaNiAl catalyst, evidencing the positive effect of preserving smaller Ni particles (∼5 nm) attributed to the confinement of the ordered mesostructure. Compared to meso-0LaNiAl catalyst, meso-3LaNiAl is more effective in suppressing the carbon deposition, demonstrating excellent anti-coking capability via La promotion.

Fig. 12. TEM images of spent catalysts and corresponding deposited carbon.

and the enhanced stability of the framework with La-promotion as shown in TPR and WXRD results.

Sintering of the metal particles and carbon deposition can be generally ascribed as the primary reasons for catalyst deactivation in reforming reactions [77,85]. For all the catalysts, due to the strong interaction between metal and support, most nickel particles behaved excellent anti-sintering performance in despite of the presence of some large particles. Additionally, in the cases of meso-xLaNiAl (x = 0 and 3), the ordered mesostructure further enhanced the resistance of sintering by the confinement effect [29,31,47]. Therefore, it is reasonable to deduce that carbon deposition is the main cause for deactivation at given conditions.

Coke formation in ESR could be derived from methane decomposition, Boudouard reaction and ethylene polymerization [86,87]. According to the previous literatures, large Ni particles favored methane decomposition and Boudouard reaction, which accounted for the large amount of carbon [88–90]. Xie et al. [91] concluded that the highly dispersed Ni particles with 3.6 nm favored in enhancing the coking resistance. In addition, the γ-Al$_2$O$_3$ with acidic surface is known to favor the formation of ethylene, which is associated to carbon formation and eventual deactivation [49]. Accordingly, Garbarino et al. [92] added La precursor to the Ni/Al$_2$O$_3$ catalyst to enhance the basic sites, thus hindering the coke formation and improving the stability. As the CO$_2$-TPD shown in Fig. 13, the 0LaNiAl catalyst only exhibits weak CO$_2$ adsorption sites at low temperatures [61]. In contrast, the CO$_2$-TPD profiles of meso-0LaNiAl and meso-3LaNiAl catalysts present CO$_2$ desorption peaks at higher temperatures and these strong basic centers of meso-3LaNiAl are 1.3-fold compared to meso-0LaNiAl. Therefore, meso-0LaNiAl and meso-3LaNiAl catalysts exhibited excellent anti-coking capability to 0LaNiAl catalyst, especially the less amount of coke close to the Ni particles, attributing to the small nickel particle size and the strong basic sites.

Furthermore, over meso-3LaNiAl catalyst, the amount of accumulated carbon was further reduced in comparison with meso-0LaNiAl, which was attributed to the positive effect of strengthened interaction and stabilized mesostructure on preventing the Ni particles from moving out of the mesopores for aggregating to large particles as shown in Fig. 12. Moreover, it has been stated that the hydrophilic oxide lanthanum oxide can improve the activation of adsorbed H$_2$O, facilitating the gasification of coke [93–95]. Additionally, the lanthanum species enhanced the adsorption of CO$_2$ as the CO$_2$-TPD results shown, which could clean the surface carbon through Eqs. (4) and (5) [49,96] to regenerate the nickel surface, resulting in the less coke and the improved stability under reforming reaction conditions.
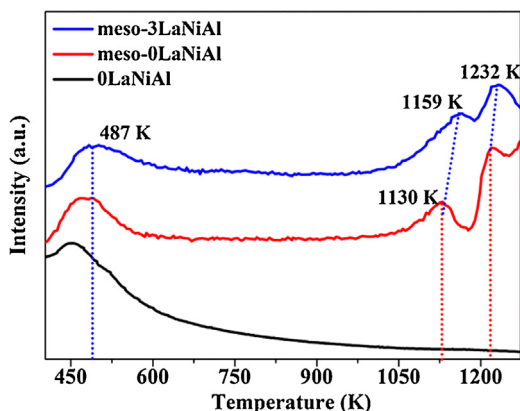
$$La_2O_3 + CO_2 = La_2O_2CO_3 \qquad (4)$$

$$La_2O_2CO_3 + C = La_2O_3 + 2CO \qquad (5)$$

Overall, the anti-sintering and anti-coking meso-3LaNiAl catalyst obtained and preserved its sufficient active surface areas, achieving improved long-term stability.

4. Conclusions

In summary, meso-xLaNiAl catalysts with ordered mesostructure have been synthesized and investigated for ESR. It was found that both the ordered mesostructure and La-modifier played significant roles in achieving excellent catalytic performance. Specifically, the ordered mesostructure was beneficial to obtain small Ni nanoparticles of 4–6 nm and to effectively stabilize the highly dispersed Ni nanoparticles due to the confinement effect, which accounted for the better catalytic performance of meso-xLaNiAl catalyst to the conventional 0LaNiAl catalyst. The La-modification could partly reconstruct the metastable Ni–Al oxides and obtain amount of easily reduced nickel species, which could be less embedded in the skeleton and thus expose more active surface atoms. Meso-3LaNiAl catalyst with appropriate amount of La achieved ~37% these Ni species, thus possessed the highest active nickel surface areas, and consequently achieved the highest initial activity at high temperatures (e.g., 873 K).

Coke deposition was the main reason for deactivation in the present work. Over 0LaNiAl catalyst with acidic surface and large nickel particles, significant amount of coke was deposited, especially close to the Ni particles, and thus led to severe deactivation. In comparison, meso-0LaNiAl catalysts obtained smaller nickel particles and certain amount of basic sites and consequently exhibited excellent anti-coking capability. Furthermore, the least amount of coke was accumulated on meso-3LaNiAl catalyst. On the one hand, the strengthened interaction and stabilized mesostructure prevented the Ni particles from moving out of the mesopores, from aggregating to large particles, and thus from coking. On the other hand, the addition of La-promoter could react with H$_2$O and CO$_2$, facilitating the removal of coke deposition and the regeneration of active nickel surface. Therefore, meso-3LaNiAl catalyst obtained and preserved its sufficient active surface areas, achieving improved long-term stability.

Acknowledgements

References

[1] M. Sanchez Sanchez, R. Navarro, J. Fierro, Catal. Today 129 (2007) 336–345.
[2] L.F. Zhang, W. Li, J. Liu, C.L. Guo, Y.P. Wang, J.L. Zhang, Fuel 88 (2009) 511–518.
[3] D. Zanchet, J.B.O. Santos, S. Damyanova, J.M.R. Gallo, J.M.C. Bueno, ACS Catal. 5 (2015) 3841–3863.
[4] A. Haryanto, S. Fernando, N. Murali, S. Adhikari, Energy Fuels 19 (2005) 2098–2106.
[5] L.V. Mattos, G. Jacobs, B.H. Davis, F.B. Noronha, Chem. Rev. 112 (2012) 4094–4123.
[6] S. Li, J. Gong, Chem. Soc. Rev. 43 (2014) 7245–7256.
[7] F. Aupretre, C. Descorme, D. Duprez, Catal. Commun. 3 (2002) 263–267.
[8] J. Llorca, N. Homs, J. Sales, P.R. de la Piscina, J. Catal. 209 (2002) 306–317.
[9] A.N. Fatsikostas, X.E. Verykios, J. Catal. 225 (2004) 439–452.
[10] V. Palma, F. Castaldo, P. Ciambelli, G. Iaquaniello, G. Capitani, Int. J. Hydrog. Energy 38 (2013) 6633–6645.
[11] V. Palma, F. Castaldo, P. Ciambelli, G. Iaquaniello, Appl. Catal. B 145 (2014) 73–84.
[12] D.K. Liguras, D.I. Kondarides, X.E. Verykios, Appl. Catal. B 43 (2003) 345–354.

Fig. 13. CO$_2$-TPD profiles of selected reduced catalysts.

[13] F. Frusteri, S. Freni, L. Spadaro, V. Chiodo, G. Bonura, S. Donato, S. Cavallaro, Catal. Commun. 5 (2004) 611–615.
[14] A.L. Alberton, M.M.V.M. Souza, M. Schmal, Catal. Today 123 (2007) 257–264.
[15] S.M. de Lima, A.M. da Silva, L.O.O. da Costa, J.M. Assaf, G. Jacobs, B.H. Davis, L.V. Mattos, F.B. Noronha, Appl. Catal. A 377 (2010) 181–190.
[16] C.X. Zhang, H.R. Yue, Z.Q. Huang, S.R. Li, G.W. Wu, X.B. Ma, J.L. Gong, ACS Sustain. Chem. Eng. 1 (2013) 161–173.
[17] M.C.J. Bradford, M.A. Vannice, Catal. Rev. Sci. Eng. 41 (1999) 1–42.
[18] J.H. Kim, D.J. Suh, T.J. Park, K.L. Kim, Appl. Catal. A 197 (2000) 191–200.
[19] D.L. Trimm, Catal. Today 49 (1999) 3–10.
[20] A. Vandillen, R. Terorde, D. Lensveld, J. Geus, K. Debjong, J. Catal. 216 (2003) 257–264.
[21] T. Roussiere, K.M. Schelkle, S. Titlbach, G. Wasserschaff, A. Milanov, G. Cox, E. Schwab, O. Deutschmann, L. Schulz, A. Jentys, J. Lercher, S.A. Schunk, ChemCatChem 6 (2014) 1438–1446.
[22] H.P. Xiao, Z.C. Liu, X.G. Zhou, K.K. Zhu, Catal. Commun. 34 (2013) 11–15.
[23] G.W. Wu, S.R. Li, C.X. Zhang, T. Wang, J.L. Gong, Appl. Catayl. B 144 (2014) 277–285.
[24] C.T. Kresge, M.E. Leonowicz, W.J. Roth, J.C. Vartuli, J.S. Beck, Nature 359 (1992) 710–712.
[25] A.J. Vizcaíno, A. Carrero, J.A. Calles, Catal. Today 146 (2009) 63–70.
[26] O.A.G. Vargas, J.A.D. Heredia, J.A. Wang, L.F. Chen, A.M. Castellanos, M.E. Llanos, Int. J. Hydrog. Energy 38 (2013) 13914–13925.
[27] A. Ungureanu, B. Dragoi, A. Chirieac, C. Ciotonea, S. Royer, D. Duprez, A.S. Mamede, E. Dumitriu, ACS Appl. Mater. Interfaces 5 (2013) 3010–3025.
[28] S. Zhang, S. Muratsugu, N. Ishiguro, M. Tada, ACS Catal. 3 (2013) 1855–1864.
[29] W.H. Shen, K. Komatsubara, T. Hagiyama, A. Yoshida, S. Naito, Chem. Commun. (2009) 6490–6492.
[30] L. Xu, H. Song, L. Chou, Appl. Catal. B 108–109 (2011) 177–190.
[31] N. Wang, Z.X. Xu, J. Deng, K. Shen, X.P. Yu, W.Z. Qian, W. Chu, F. Wei, ChemCatChem 6 (2014) 1470–1480.
[32] Z.X. Li, F.B. Shi, L.L. Li, T. Zhang, C.H. Yan, Phys. Chem. Chem. Phys. 13 (2011) 2488–2491.
[33] V. Subramanian, E.S. Gnanakumar, D.W. Jeong, W.B. Han, C.S. Gopinath, H.S. Roh, Chem. Commun. 49 (2013) 11257–11259.
[34] W.H. Shen, H. Momoi, K. Komatsubara, T. Saito, A. Yoshida, S. Naito, Catal. Today 171 (2011) 150–155.
[35] F. Frusteri, S. Freni, V. Chiodo, L. Spadaro, O. Di Blasi, G. Bonura, S. Cavallaro, Appl. Catal. A 270 (2004) 1–7.
[36] H.-S. Roh, A. Platon, Y. Wang, D.L. King, Catal. Lett. 110 (2006) 1–6.
[37] A. Iriondo, V.L. Barrio, J.F. Cambra, P.L. Arias, M.B. Guemez, R.M. Navarro, M.C. Sanchez Sanchez, J.L.G. Fierro, Top. Catal. 49 (2008) 46–58.
[38] K.F.M. Elias, A.F. Lucredio, E.M. Assaf, Int. J. Hydrog. Energy 38 (2013) 4407–4417.
[39] L. Garcia, R. French, S. Czernik, E. Chornet, Appl. Catal. A 201 (2000) 225–239.
[40] Z.W. Liu, H.S. Roh, K.W. Jun, J. Ind. Eng. Chem. 9 (2003) 267–274.
[41] M. Sanchez Sanchez, R. Navarro, J. Fierro, Int. J. Hydrog. Energy 32 (2007) 1462–1471.
[42] X.Y. Chen, Y. Liu, G.X. Niu, Z.X. Yang, M.Y. Bian, A. He, Appl. Catal. A 205 (2001) 159–172.
[43] H.G.J. Lansink Rotgerink, R.P.A.M. Paalman, J.G. Van Ommen, J.R.H. Ross, Appl. Catal. 45 (1988) 257–280.
[44] Y.J. Hou, Y.Q. Wang, F. He, W.L. Mi, Z.H. Li, Z.T. Mi, W. Wu, E.Z. Min, Appl. Catal. A 259 (2004) 35–40.
[45] R. Martinez, E. Romero, C. Guimon, R. Bilbao, Appl. Catal. A 274 (2004) 139–149.
[46] Q. Yuan, A.X. Yin, C. Luo, L.D. Sun, Y.W. Zhang, W.T. Duan, H.C. Liu, C.H. Yan, J. Am. Chem. Soc. 130 (2008) 3465–3472.
[47] S.M. Morris, P.F. Fulvio, M. Jaroniec, J. Am. Chem. Soc. 130 (2008) 15210–15216.
[48] L.L. Xu, Z.C. Miao, H.L. Song, W. Chen, L.J. Chou, Catal. Sci. Technol. 4 (2014) 1759–1770.
[49] R.C. Cerritos, R.F. Ramirez, A.F.A. Alvarado, J.M.M. Rosales, T.V. Garcia, I.R.G. Esquivel, Ind. Eng. Chem. Res. 50 (2011) 2576–2584.
[50] K.W. Siew, H.C. Lee, J. Gimbuna, C.K. Cheng, J. Energy Chem. 23 (2014) 15–21.
[51] C.H. Bartholomew, R.B. Pannell, J. Catal. 65 (1980) 390–401.
[52] C.X. Zhang, S.R. Li, G.W. Wu, J.L. Gong, Catal. Today 233 (2014) 53–60.
[53] D. Li, L. Zeng, X. Li, X. Wang, H. Ma, S. Assabumrungrat, J. Gong, Appl. Catal. B 176 (2015) 532–541.
[54] N. Wang, K. Shen, L.H. Huang, X.P. Yu, W.Z. Qian, W. Chu, ACS Catal. 3 (2013) 1638–1651.
[55] R.E.C.M. Bettman, K. Otto, W.H. Weber, J. Catal. 117 (1989) 447–454.
[56] K.S.W. Sing, Pure Appl. Chem. 54 (1982) 2201–2218.
[57] J.T. Richardson, M.V. Twingg, Appl. Catal. A 167 (1998) 57–64.
[58] B. Scheffer, P. Molhoek, J. Moulijn, Appl. Catal. 46 (1989) 11–30.
[59] J.M. Rynkowski, T. Paryjczak, M. Lenik, Appl. Catal. A 106 (1993) 73–82.
[60] L.L. Xu, H.L. Song, L.J. Chou, Catal. Sci. Technol. 1 (2011) 1032–1042.
[61] L.L. Xu, H.L. Song, L.J. Chou, ACS Catal. 2 (2012) 1331–1342.
[62] C. Li, Y.-W. Chen, Thermochim. Acta 256 (1995) 457–465.
[63] A. Serrano-Lotina, A.J. Martin, M.A. Folgado, L. Daza, Int. J. Hydrog. Energy 37 (2012) 12342–12350.
[64] Q.P. Sun, Y. Zheng, Y. Zheng, Y.H. Xiao, G.H. Cai, K.M. Wei, Scr. Mater. 65 (2011) 1026–1029.
[65] S.R. Li, C.X. Zhang, Z.Q. Huang, G.W. Wu, J.L. Gong, Chem. Commun. 49 (2013) 4226–4228.
[66] F. Wang, L. Xu, J. Zhang, Y. Zhao, H. Li, H.X. Li, K. Wu, G.Q. Xu, W. Chen, Appl. Catal. B 180 (2016) 511–520.
[67] A. Denis, W. Grzegorczyk, W. Gac, A. Machocki, Catal. Today 137 (2008) 453–459.
[68] M. Bilal, S.D. Jackson, Catal. Sci. Technol. 3 (2013) 754–766.
[69] L. Liu, X. Ma, J. Li, Int. J. Energy Res. 38 (2014) 860–874.
[70] G. Garbarino, C. Wang, I. Valsamakis, S. Chitsazan, P. Riani, E. Finocchio, M. Flytzani-Stephanopoulos, G. Busca, Appl. Catal. B 174–175 (2015) 21–34.
[71] V. Nichele, M. Signoretto, F. Menegazzo, A. Gallo, V. Dal Santo, G. Cruciani, G. Cerrato, Appl. Catal. B 111–112 (2012) 225–232.
[72] M. Benito, J.L. Sanz, R. Isabel, R. Padilla, R. Arjona, L. Daza, J. Power Sources 151 (2005) 11–17.
[73] A. Erdőhelyi, Catalysis for Alternative Energy Generation, in: L. Guczi, A. Erdőhelyi (Eds.), Springer, New York, 2012, pp. 128–173.
[74] S.M. Kim, S.I. Woo, ChemSusChem 5 (2012) 1513–1522.
[75] K.W. Siew, H.C. Lee, J. Gimbun, S.Y. Chin, M.R. Khan, Y.H. Taufiq-Yap, C.K. Cheng, Renew. Energy 74 (2015) 441–447.
[76] Y. Cui, H. Zhang, H. Xu, W. Li, Appl. Catal. A 331 (2007) 60–69.
[77] P.D. Vaidya, A.E. Rodrigues, Chem. Eng. J. 117 (2006) 39–49.
[78] H.-S.R. Zhongwen Liu, Ki-Won Jun, J. Ind. Eng. Chem. 3 (2003) 267–274.
[79] T. Montini, R. Singh, P. Das, B. Lorenzut, N. Bertero, P. Riello, A. Benedetti, G. Giambastiani, C. Bianchini, S. Zinoviev, S. Miertus, P. Fornasiero, ChemSusChem 3 (2010) 619–628.
[80] Y. Kathiraser, W. Thitsartarn, K. Sutthiumporn, S. Kawi, J. Phys. Chem. C 117 (2013) 8120–8130.
[81] J.A. Calles, A. Carrero, A.J. Vizcaíno, L. García-Moreno, Catal. Today 227 (2014) 198–206.
[82] H.M. Swaan, V.C.H. Kroll, G.A. Martin, C. Mirodatos, Catal. Today 21 (1994) 571–578.
[83] S. Wang, G.Q.M. Lu, Appl. Catal. B 16 (1998) 269–277.
[84] S.M. Stagg-Williams, F.B. Noronha, G. Fendley, D.E. Resasco, J. Catal. 194 (2000) 240–249.
[85] I. Rossetti, C. Biffi, C.L. Bianchi, V. Nichele, M. Signoretto, F. Menegazzo, E. Finocchio, G. Ramis, A. Di Michele, Appl. Catal. B 117 (2012) 384–396.
[86] L.P.R. Profeti, J.A.C. Dias, J.M. Assaf, E.M. Assaf, J. Power Sources 190 (2009) 525–533.
[87] C. Zhang, H. Yue, Z. Huang, S. Li, G. Wu, X. Ma, J. Gong, ACS Sustain. Chem. Eng. 1 (2013) 161–173.
[88] M.A. Goula, A.A. Lemonidou, A.M. Efstathiou, J. Catal. 161 (1996) 626–640.
[89] Z.Y. Hou, J. Gao, J.Z. Guo, D. Liang, H. Lou, X.M. Zheng, J. Catal. 250 (2007) 331–341.
[90] W.J. Cai, L.P. Qian, B. Yue, H.Y. He, Chin. Chem. Lett. 25 (2014) 1411–1415.
[91] T. Xie, L. Shi, J. Zhang, D. Zhang, Chem. Commun. 50 (2014) 7250–7253.
[92] G. Garbarino, C. Wang, I. Valsamakis, S. Chitsazan, P. Riani, E. Finocchio, M. Flytzani-Stephanopoulos, G. Busca, Appl. Catal. B 174–175 (2015) 21–34.
[93] L.A. Garcia, R. French, S. Czernik, E. Chornet, Appl. Catal. A 201 (2000) 225–239.
[94] X. Hu, G. Lu, Catal. Commun. 12 (2010) 50–53.
[95] D.A. Constantinou, M.C. Álvarez-Galván, J.L.G. Fierro, A.M. Efstathiou, Appl. Catal. B 117–118 (2012) 81–95.
[96] L. Bednarczuk, P. Ramírez de la Piscina, N. Homs, Int. J. Hydrog. Energy 40 (2015) 5256–5263.